Available online at www.sciencedirect.com

ScienceDirect

Journal of Sound and Vibration 322 (2009) 883–900

JOURNAL OF SOUND AND VIBRATION

www.elsevier.com/locate/jsvi

Exact acoustical analysis of vibrating rectangular plates with two opposite edges simply supported via Mindlin plate theory

Sh. Hosseini Hashemi[a], K. Khorshidi[b,*], H. Rokni Damavandi Taher[a]

[a]*Impact Research Laboratory, School of Mechanical Engineering, Iran University of Science and Technology, Narmak, Tehran 16846-13114, Iran*

[b]*School of Engineering, Arak University, Shariaty Street, Arak 38138-5-3945, Iran*

Received 5 December 2006; received in revised form 20 November 2008; accepted 23 November 2008
Handling Editor: A.V. Metrikine
Available online 13 January 2009

Abstract

This study investigates acoustic radiation of rectangular Mindlin plates in different combinations of classical boundary conditions. A set of exact close-form sound pressure equations are given for the first time using the so-called Mindlin plate theory (a first-order shear deformation theory) for the plates having two opposite edges that are simply supported. The other two edges may be given any possible combination of free, simply-supported and clamped boundary conditions. It is assumed that no fluid loading occurs on the plate structure. In order to study the transverse vibration of moderately thick rectangular plates, the dimensionless equations of motion are derived based on the Mindlin plate theory. Structural–acoustic coupling is implemented for vibrating plate models. The radiation field of a vibrating plate with a specified distribution of velocity on the surface can be computed using the Rayleigh integral approach. The acoustic pressure distribution of the radiator is analytically obtained in its far field. To reveal the excellent accuracy of our exact acoustical solution, a comparison is first made with the existing data. Additionally, a few 3-D plots of the directivity pattern and their corresponding contour plots are illustrated for moderately thick rectangular plates with different boundary conditions. Finally, the influence of six possible combinations of boundary conditions, aspect ratios and thickness to length ratios on the sound pressure, frequency and critical distance parameters are examined and discussed in detail.

1. Introduction

Rectangular plates are important structural elements. They are used in a wide range of applications in many branches of modern technology, namely mechanical, aerospace, electronic, marine, optical, nuclear and structural engineering. The typical thickness of practical components is often beyond the thin plate theory limit and this may have a considerable effect on sound radiation. Although there is a substantial body of literature on the structural dynamics of thin and thick plates [1–5], acoustic radiation from thick plates has not been adequately examined.

---

*Corresponding author. Tel.: +98 911 154 0318; fax: +98 861 222 5946.
E-mail address: k-khorshidi@araku.ac.ir (K. Khorshidi).

0022-460X/$ - see front matter © 2008 Elsevier Ltd. All rights reserved.
doi:10.1016/j.jsv.2008.11.042

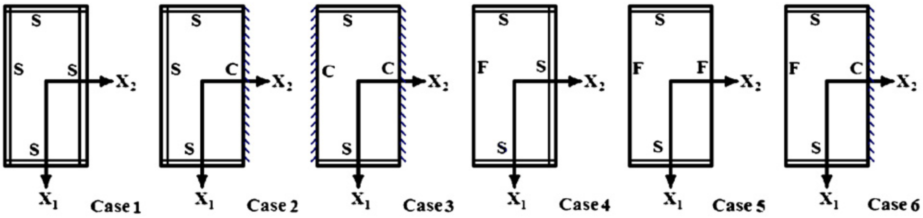

Fig. 1. Six combinations of classical boundary conditions at the edges of rectangular Mindlin plates.

Early research efforts to calculate the radiated sound field for a flat plate in an infinite baffle dates back to the work of Rayleigh [6]. Lomas and Hayek [7] developed the Green function solution for the steady-state vibrations of an elastically supported rectangular plate coupled to a semi-infinite acoustic medium. Cremer and Heckl [8] analyzed sound radiation of a planar source using a Fourier transformation approach in *K*-space (wavenumber space). Williams [9] proposed a series expansion in ascending power of the wavenumber *K* for the acoustic power radiated from a planar source.

Sound radiation from thin circular and annular disks was examined by Lee and Singh [10]. They focused on either flexural vibration modes or rigid body piston motions. Tao et al. [11] presented the mathematical expression for sound radiation from a thin infinite isotropic plate coupled with light and heavy fluids and subjected to multipoint excitation. Recently, Lin [12,13] studied the acoustic field of circular and rectangular radiators in flexural vibration. The radiator was considered to be a rectangular thin plate in flexural vibration with simply supported boundary conditions [13]. The acoustic pressure distribution of the radiator in a far field was analytically obtained and its near field was numerically computed. Zhou et al. [14] calculated the sound pressure at the far field from a thin infinite plate in contact with a layered inhomogeneous fluid subjected to single point excitation. Musha [15] presented a new numerical calculation method based on the Rayleigh integral to obtain the instantaneous radiation pattern by using the harmonic wavelet transformation for a rectangular vibrating plate. More recently, Lee and Singh [16] presented two analytical solutions for the far-field modal sound pressure radiation from the radial structural modes of a thick annular disk with completely free boundary conditions.

The exact analysis of sound radiation of thin rectangular plates having four simply supported edges can be found in Lin's work [13]. Such equations for moderately thick plates are not available in the literature. In order to fill this apparent void, the present work is carried out by providing the exact acoustical analysis for six cases of a rectangular plate having two opposite sides simply supported. The six cases considered in this study include S–S–S–S, S–C–S–S, S–C–S–C, S–S–S–F, S–F–S–F and S–C–S–F rectangular Mindlin plates, as shown in Fig. 1. The integrated equations of motion in terms of the resultant stresses are derived based on Mindlin plate theory for moderately thick rectangular plates. This is done by considering transverse shear deformation and rotary inertia [17]. The exact transverse deflection and the exact displacements along X_1- and X_2-axes are derived for the first time. The acoustic pressure distribution of the radiator in its far field is analytically obtained using a Rayleigh integral approach. After performing a comparison study, it is proven that the Mindlin plate theory and its results may be considered for thin plates. Some numerical results are presented for the acoustic pressure of the plate in the far field as mode shapes. The influence of six possible combinations of boundary conditions, aspect ratios and thickness to length ratios on the sound pressure, frequency and critical distance parameters is graphically investigated. In the future, these results may serve as benchmark solutions for validating approximate 2-D theories and new computational techniques.

2. Equations of vibratory motion of moderately thick plates

Consider a flat, isotropic, rectangular Mindlin plate of uniform thickness h, length a, width b and Poisson's ratio v described in the Cartesian coordinate system (x_1, x_2, x_3), as depicted in Fig. 2(a). The Cartesian coordinates system (X_1, X_2, X_3) in Fig. 2(b) is a dimensionless coordinate system, where $X_1 = x_1/a$, $X_2 = x_2/b$ and $X_3 = x_3$.

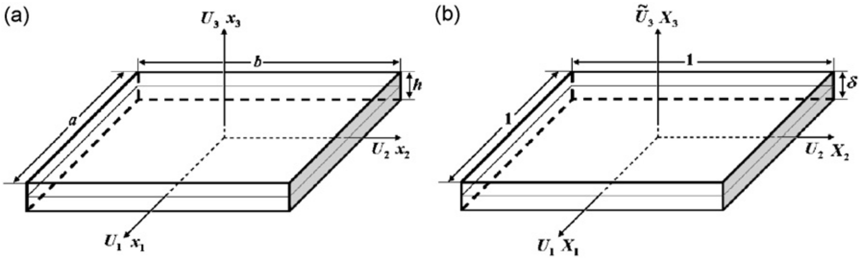

Fig. 2. A rectangular Mindlin plate with coordinate convention: (a) dimensional coordinate system and (b) non-dimensional coordinate system.

Based on dimensionless parameters, the transverse deflection for each of the six considered cases can be obtained by following the research work of Hosseini-Hashemi and Arsanjani [17]. In particular, for S–S–S–S cases, it can be calculated as

$$\tilde{U}_3 = A_1 \sin(\lambda_1(X_2 + 1/2)) \sin(\mu(X_1 + 1/2)), \tag{1}$$

where $\tilde{U}_3 = U_3/a$ is the dimensionless transverse deflection of the plate, $\mu = m\pi$ $(m = 1, 2, \ldots)$, A_1 is the arbitrary constant (see Appendix A for more details) and λ_1 is a constant depending on geometry parameters and material properties of the plate.

Hereafter, some constant parameters, including λ_2, λ_3, C_1, C_2 and L_i $(i = 1, 2, 3 \text{ and } 4)$, are employed to extract transverse deflection of the plate. These constants are dependent on the geometry parameters and material properties of the plate.

For the case of S–C–S–S:

$$\tilde{U}_3 = A_1 \left[\sin(\lambda_1(X_2 + 1/2)) - \frac{\sin(\lambda_1)}{\sinh(\lambda_2)} \sinh(\lambda_2(X_2 + 1/2))\right] \sin(\mu(X_1 + 1/2)). \tag{2}$$

For the case of S–C–S–C:

$$\begin{aligned} \tilde{U}_3 = A_1 \Big[&\sin(\lambda_1(X_2 + 1/2)) + b_1 \cos(\lambda_1(X_2 + 1/2)) - (b_1 \cos(\lambda_1) - b_1 \cosh(\lambda_2) \\ &+ \sin(\lambda_1)) \frac{\sinh(\lambda_2(X_2 + 1/2))}{\sinh(\lambda_2)} - b_1 \cosh(\lambda_2(X_2 + 1/2))\Big] \sin(\mu(X_1 + 1/2)), \end{aligned} \tag{3}$$

where

$$b_1 = -\frac{\eta^2 \lambda_3 (C_2 \lambda_2 \sin(\lambda_1) - C_1 \lambda_1 \sinh(\lambda_2)) \sinh(\lambda_3) + (C_1 - C_2)\mu^2 \sin(\lambda_1) \sinh(\lambda_2)}{C_2 \eta^2 \lambda_2 \lambda_3 (\cos(\lambda_1) - \cosh(\lambda_2)) \sinh(\lambda_3) + (C_1 - C_2)\mu^2 (\cos(\lambda_1) - \cosh(\lambda_3)) \sinh(\lambda_2)} \tag{4}$$

and $\eta = a/b$ is the aspect ratio.

For the case of S–S–S–F:

$$\begin{aligned} \tilde{U}_3 = A_1 \Big\{&[\sin(\lambda_1(X_2 + 1/2)) + b_2 \cos(\lambda_1(X_2 + 1/2))] \cosh(\lambda_2) + \frac{L_1 \lambda_1}{L_3 \lambda_2} \sinh[\lambda_2(1/2 - X_2)] \\ &- (b_2 \cos(\lambda_1) + \sin(\lambda_1)) \cosh(\lambda_2(X_2 + 1/2))\Big\} \frac{\sin(\mu(X_1 + 1/2))}{\cosh(\lambda_2)}, \end{aligned} \tag{5}$$

where

$$b_2 = -\frac{R_1}{R_2}, \tag{6}$$

$$\begin{aligned} R_1 = {} & C_2 L_2 (L_3 \lambda_2 \sin(\lambda_1) - L_1 \lambda_1 \sinh(\lambda_2)) \cosh(\lambda_3) \\ & + (C_1 - C_2) \lambda_2 \mu^2 (1 - v)(L_3 \sin(\lambda_1) + 2\eta^2 \lambda_1 \lambda_3 \sinh(\lambda_3)) \cosh(\lambda_2), \end{aligned} \tag{7}$$

$$R_2 = L_3 \lambda_2 \{C_2 L_2 \cos(\lambda_1) \cosh(\lambda_3) + [(C_1 - C_2)\mu^2 (1 - v) \cos(\lambda_1) + C_1 L_4 \cosh(\lambda_3)] \cosh(\lambda_2)\}. \tag{8}$$

For the case of S–F–S–F:

$$\begin{aligned}\tilde{U}_3 = A_1\Bigg[&\sin(\lambda_1(X_2+1/2)) + b_3\cos(\lambda_1(X_2+1/2)) - \frac{L_1\lambda_1}{L_3\lambda_2}\sinh(\lambda_2(X_2+1/2))\\ &+ b_4\cosh(\lambda_2(X_2+1/2))\Bigg]\sin(\mu(X_1+1/2)),\end{aligned} \tag{9}$$

where

$$b_3 = -\frac{R_3}{R_4}, \quad b_4 = \frac{R_5}{R_6}, \tag{10}$$

$$\begin{aligned}R_3 = {}& 2(C_1-C_2)\eta^2\mu^2\lambda_1\lambda_2\lambda_3(1-\nu)(\cos(\lambda_1)-\cosh(\lambda_3))\sinh(\lambda_2)\\ &- C_2L_1L_2\lambda_1(\cos(\lambda_1)-\cosh(\lambda_2))\sinh(\lambda_3),\end{aligned} \tag{11}$$

$$\begin{aligned}R_4 = {}& C_2L_1L_2\lambda_1\sin(\lambda_1)\sinh(\lambda_3) - \lambda_2[2(C_1-C_2)\eta^2\mu^2\lambda_1\lambda_3(1-\nu)\sin(\lambda_1)\\ &+ C_1L_3L_4\sinh(\lambda_3)]\sinh(\lambda_2),\end{aligned} \tag{12}$$

$$\begin{aligned}R_5 = {}& \eta^2\lambda_1\lambda_3(1-\nu)[(C_2-1)L_1(\cosh(\lambda_2)-\cosh(\lambda_3))\\ &+ (C_1-1)L_3(b_3\sin(\lambda_1)-\cos(\lambda_1)+\cosh(\lambda_3))] - b_3C_1L_3L_4\sinh(\lambda_3),\end{aligned} \tag{13}$$

$$R_6 = L_3[(C_2-1)\eta^2\lambda_2\lambda_3(1-\nu)\sinh(\lambda_2) - C_2L_2\sinh(\lambda_3)]. \tag{14}$$

For the case of S–C–S–F:

$$\begin{aligned}\tilde{U}_3 = A_1\Bigg\{&[\sin(\lambda_1(X_2+1/2)) + b_5\cos(\lambda_1(X_2+1/2))]\cosh(\lambda_2) + \frac{L_1\lambda_1}{L_3\lambda_2}\sinh[\lambda_2(1/2-X_2)]\\ &-(b_5\cos(\lambda_1)+\sin(\lambda_1))\cosh(\lambda_2(X_2+1/2))\Bigg\}\frac{\sin(\mu(X_1+1/2))}{\cosh(\lambda_2)},\end{aligned} \tag{15}$$

where

$$b_5 = -\frac{R_7}{R_8}, \tag{16}$$

$$\begin{aligned}R_7 = {}& C_2L_2(L_3\lambda_2\sin(\lambda_1) - L_1\lambda_1\sinh(\lambda_2))\cosh(\lambda_3)\\ &+ (C_1-C_2)\mu^2\lambda_2(1-\nu)(L_3\sin(\lambda_1) + 2\eta^2\lambda_1\lambda_3\sinh(\lambda_3))\cosh(\lambda_2),\end{aligned} \tag{17}$$

$$\begin{aligned}R_8 = L_3\lambda_2[&(C_1-C_2)\mu^2(1-\nu)\cos(\lambda_1)\cosh(\lambda_2)\\ &+ (C_2L_2\cos(\lambda_1) + C_1L_4\cosh(\lambda_2))\cosh(\lambda_3)],\end{aligned} \tag{18}$$

where

$$C_1 = 1 - \frac{\alpha_2^2}{\nu_1\alpha_3^2}, \quad C_2 = 1 - \frac{\alpha_1^2}{\nu_1\alpha_3^2},$$

$$\alpha_1^2 \text{ and } \alpha_2^2 = \frac{\beta^2}{2}\left[\frac{\delta^2}{12}\left(\frac{1}{\kappa^2\nu_1}+1\right) \pm \sqrt{\left(\frac{\delta^2}{12}\right)^2\left(\frac{1}{\kappa^2\nu_1}-1\right)^2 + \frac{4}{\beta^2}}\right],$$

$$\alpha_3^2 = \frac{12\kappa^2}{\beta^2\delta^2}\alpha_1^2\alpha_2^2 = \frac{12\kappa^2}{\delta^2}\left(\frac{\beta^2\delta^4}{144\kappa^2\nu_1}-1\right) \tag{19}$$

and $\beta = \omega a^2\sqrt{\rho h/D}$ is the dimensionless frequency parameter, ω and ρ are the circular natural frequency and the mass density, respectively, $D = Eh^3/(12(1-\nu^2))$ is the flexural rigidity, κ and E are the shear correction factor and the modulus of elasticity, respectively, $\delta = h/a$ is the thickness to length ratio and $v_1 = (1 - v)/2$. It is also possible to define

$$L_1 = (C_1 - 1)\eta^2\lambda_3^2 - (C_1 + 1)\mu^2, \quad L_2 = \eta^2\lambda_2^2 - v\mu^2,$$

$$L_3 = (C_2 - 1)\eta^2\lambda_3^2 - (C_2 + 1)\mu^2, \quad L_4 = \eta^2\lambda_1^2 + v\mu^2, \tag{20}$$

where λ_1, λ_2 and λ_3 are related to α_1, α_2 and α_3, respectively, by

$$\lambda_1 = \frac{1}{\eta}\sqrt{\alpha_1^2 - \mu^2}, \quad \lambda_2 = \frac{1}{\eta}\sqrt{-\alpha_2^2 + \mu^2}, \quad \lambda_3 = \frac{1}{\eta}\sqrt{-\alpha_3^2 + \mu^2}. \tag{21}$$

Coefficients λ_1, λ_2 and λ_3 can also be expressed as

$$\lambda_1^2 = \frac{-\lambda + \sqrt{\lambda^2 - 4\alpha}}{2}, \quad \lambda_2^2 = \frac{\lambda + \sqrt{\lambda^2 - 4\alpha}}{2}, \quad \lambda_3 = \frac{1}{\eta}\sqrt{\mu^2 - \kappa^2\beta^2/\theta + \theta/v_1}, \tag{22}$$

where

$$\lambda = \frac{a_1\mu^2 + a_2\mu^2 - a_3 - a_5}{a_2\eta^2}, \quad \alpha = \frac{a_1\mu^4 - (a_3 + a_4)\mu^2 + a_6}{a_2\eta^4}, \tag{23}$$

a_i $(i = 1, 2, \ldots, 6)$ are constants defined as

$$a_1 = a_2 = 1, \quad a_3 = \frac{1}{\theta}(\beta^2), \quad a_4 = a_5 = \frac{\beta^2\kappa^2\upsilon_1}{\theta}, \quad a_6 = \left(\frac{\beta^2\kappa^2\upsilon_1}{\theta^2} - 1\right)\beta^2 \tag{24}$$

and

$$\theta = 12\frac{\kappa^2 v_1}{\delta^2}. \tag{25}$$

3. Equations of acoustical radiation field of moderately thick plates

Assuming free harmonic motion, the velocity distribution on the surface of the plate may be written as

$$\tilde{V}(X_1, X_2, \tilde{t}) = \mathrm{j}\beta\tilde{U}_3(X_1, X_2)\mathrm{e}^{\mathrm{j}\beta\tilde{t}}, \tag{26}$$

where $\tilde{t} = (t\sqrt{D/\rho h})/a^2$ is the dimensionless time, t is the time and $\mathrm{j} = \sqrt{-1}$. Here we assume that the rectangular moderately thick plate radiator in flexural vibration is mounted on a flat rigid baffle of infinite extent. The coordinates shown in Fig. 3 are positioned in the mid-plane surface of the plate. The acoustic pressure at the field point $P'(X_{1p}, X_{2p}, X_{3p})$ can be obtained by dividing the radiating surface of the flexural

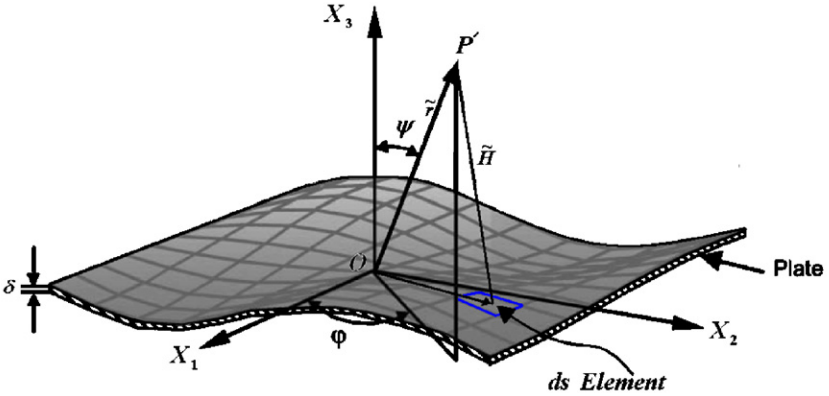

Fig. 3. A rectangular plate and its field point in the spherical coordinate system.

plate into infinitesimal elements ($\mathrm{d}s = \mathrm{d}X_1\,\mathrm{d}X_2$), where each element acts as a simple baffled source of strength having midpoint coordinates (X_{1s}, X_{2s}).

The distance between the midpoint of the infinitesimal elements ($\mathrm{d}s$) and the observation point (P') may be given by

$$\tilde{H} = \sqrt{(X_{1p} - X_{1s})^2 + (X_{2p} - X_{2s})^2 + X_{3p}^2}. \tag{27}$$

The position of the observation point can also be expressed in its spherical coordinates

$$X_{1p} = \tilde{r}\,\sin(\psi)\cos(\phi), \quad X_{2p} = \tilde{r}\,\sin(\psi)\sin(\phi), \quad X_{3p} = \tilde{r}\,\cos(\psi), \tag{28}$$

where $\tilde{r}$ is the distance between the center of the spherical coordinates and the observation point

$$\tilde{r} = \sqrt{X_{1p}^2 + X_{2p}^2 + X_{3p}^2}. \tag{29}$$

Based on the theory of a Rayleigh integral [18], the total dimensionless acoustic pressure is

$$\tilde{P} = -\frac{\tilde{K}\tilde{\rho}_0\tilde{C}_0\beta}{2\pi}\int\int\frac{\tilde{U}_3}{\tilde{H}}\mathrm{e}^{\mathrm{j}(\beta\tilde{t}-\tilde{K}\tilde{H})}\,\mathrm{d}X_1\,\mathrm{d}X_2, \tag{30}$$

where $\tilde{P} = Pa^2\eta h/D$, $\tilde{K} = \beta/\tilde{C}_0$, $\tilde{\rho}_0 = \rho_0/\rho$, ρ_0, $\tilde{C}_0 = C_0 a\sqrt{\rho h/D}$ and C_0 are the dimensionless sound pressure, wavenumber, dimensionless density, density of the medium, dimensionless speed of sound in medium and speed of sound in medium, respectively.

The critical distance $\tilde{D}_c$ between the near and the far fields for a rectangular plate radiator as given by Kirkup [18] may be approximated as

$$\tilde{D}_c \geqslant 1/\tilde{\lambda}, \tag{31}$$

where $\tilde{\lambda} = \tilde{C}_0/\tilde{f}$ is the dimensionless wavelength and $\tilde{f} = \beta/2\pi$ is the dimensionless frequency of the radiated sound that is also equal to the resonance frequency of the rectangular plate in the flexural vibration. Using the far-field approximation, the distance $\tilde{H}$ in the acoustic pressure amplitude can be approximated as $\tilde{r}$. The effect of distance on the phase of the acoustic pressure can be approximately expressed as

$$\tilde{H} = \tilde{r} - \sin(\psi)\cos(\phi)X_1 - \sin(\psi)\sin(\phi)\,X_2. \tag{32}$$

Then, Eq. (30) for far acoustic fields leads to

$$\tilde{P} = -\frac{\tilde{K}\tilde{\rho}_0\tilde{C}_0\beta}{2\pi\tilde{r}}\mathrm{e}^{\mathrm{j}(\beta\tilde{t}-\tilde{K}\tilde{r})}\int_{-0.5}^{0.5}\int_{-0.5}^{0.5}\tilde{U}_3\mathrm{e}^{\mathrm{j}\tilde{K}(\sin(\psi)\cos(\phi)X_1+\sin(\psi)\sin(\phi)X_2)}\,\mathrm{d}X_1\,\mathrm{d}X_2. \tag{33}$$

Substituting the expression of the transverse displacement distribution into Eq. (33) and separating terms of X_1 and X_2 variables, we have

$$\tilde{P} = -\frac{\tilde{K}\tilde{\rho}_0\tilde{C}_0\beta}{2\pi\tilde{r}}\mathrm{e}^{\mathrm{j}(\beta\tilde{t}-\tilde{K}\tilde{r})}A_1\int_{-0.5}^{0.5}P(X_1)\,\mathrm{d}X_1\int_{-0.5}^{0.5}P(X_1)\,\mathrm{d}X_2. \tag{34}$$

Starting from Eq. (34), it is possible to calculate $\tilde{P}$ for the six considered cases of different boundary conditions.

In particular, for the case of S–S–S–S

$$P(X_1) = \sin(\mu(X_1 + 0.5))\mathrm{e}^{\mathrm{j}\tilde{K}(\sin(\psi)\cos(\phi)X_1)},$$

$$P(X_2) = \sin(\lambda_1(X_2 + 0.5))\mathrm{e}^{\mathrm{j}\tilde{K}(\sin(\psi)\sin(\phi)X_2)} \tag{35}$$

and finally

$$P_1(\psi,\phi) = \int_{-0.5}^{0.5}P(X_1)\,\mathrm{d}X_1 = \frac{m\pi((-1)^m\mathrm{Exp}[\mathrm{j}\tilde{K}\,\cos(\gamma_1)] - 1)}{(\tilde{K}\,\cos(\gamma_1))^2 - (m\pi)^2}\mathrm{Exp}[-\mathrm{j}\tilde{K}\,\cos(\gamma_1)/2],$$

$$P_2(\psi,\phi)=\int_{-0.5}^{0.5}P(X_2)\,\mathrm{d}X_2=Z_1\mathrm{Exp}[-\mathrm{j}\tilde{K}\cos(\gamma_2)/2], \tag{36}$$

where

$$Z_1=\frac{-\lambda_1+\mathrm{Exp}[\mathrm{j}\tilde{K}\cos(\gamma_2)]\{\lambda_1\cos(\lambda_1)-\mathrm{j}\tilde{K}\cos(\gamma_2)\sin(\lambda_1)\}}{(\tilde{K}\cos(\gamma_2))^2-(\lambda_1)^2}, \tag{37}$$

$$\cos(\gamma_1)=\sin(\psi)\cos(\phi),\quad \cos(\gamma_2)=\sin(\psi)\sin(\phi). \tag{38}$$

Due to the mathematical similarity of the other five cases, $P_1(\psi,\phi)$ can be obtained using Eq. (36); however, $P_2(\psi,\phi)$ must be recalculated for each type of boundary condition.

For the case of S–C–S–S:

$$P_2(\psi,\phi)=\left[Z_1-\frac{\sin(\lambda_1)}{\sinh(\lambda_2)}Z_2\right]\mathrm{Exp}[-\mathrm{j}\tilde{K}\cos(\gamma_2)/2], \tag{39}$$

where

$$Z_2=\frac{-\lambda_2+\mathrm{Exp}[\mathrm{j}\tilde{K}\cos(\gamma_2)]\{\lambda_2\cosh(\lambda_2)-\mathrm{j}\tilde{K}\cos(\gamma_2)\sinh(\lambda_2)\}}{(\tilde{K}\cos(\gamma_2))^2+(\lambda_2)^2}. \tag{40}$$

For the case of S–C–S–C:

$$P_2(\psi,\phi)=\left[Z_1+b_1Z_3-\frac{(b_1\cos(\lambda_1)-b_1\cosh(\lambda_2)+\sin(\lambda_1))}{\sinh(\lambda_2)}Z_2-b_1Z_4\right]\mathrm{Exp}[-\mathrm{j}\tilde{K}\cos(\gamma_2)/2], \tag{41}$$

where

$$Z_3=\frac{\tilde{K}\cos(\gamma_2)+\mathrm{Exp}[\mathrm{j}\tilde{K}\cos(\gamma_2)]\{-\tilde{K}\cos(\gamma_2)\cos(\lambda_1)+\mathrm{j}\lambda_1\sin(\lambda_1)\}}{(\tilde{K}\cos(\gamma_2))^2-(\lambda_1)^2}, \tag{42}$$

$$Z_4=\frac{\mathrm{j}\tilde{K}\cos(\gamma_2)+\mathrm{Exp}[\mathrm{j}\tilde{K}\cos(\gamma_2)]\{\lambda_2\sinh(\lambda_2)-\mathrm{j}\tilde{K}\cos(\gamma_2)\cosh(\lambda_2)\}}{(\tilde{K}\cos(\gamma_2))^2+(\lambda_2)^2}. \tag{43}$$

For the case of S–S–S–F:

$$P_2(\psi,\phi)=\left[Z_1+b_2Z_3+\frac{L_1\lambda_1}{L_3\lambda_2\cosh(\lambda_2)}Z_5-\frac{(b_2\mathrm{Cos}(\lambda_1)+\sin(\lambda_1))}{\cosh(\lambda_2)}Z_4\right][-\mathrm{j}\tilde{K}\cos(\gamma_2)/2], \tag{44}$$

where

$$Z_5=\frac{\lambda_2(-\mathrm{Exp}[\mathrm{j}\tilde{K}\cos(\gamma_2)]+\cosh(\lambda_2))+\mathrm{j}\tilde{K}\cos(\gamma_2)\sinh(\lambda_2)}{(\tilde{K}\cos(\gamma_2))^2+(\lambda_2)^2}. \tag{45}$$

For the case of S–F–S–F:

$$P_2(\psi,\phi)=\left[Z_1+b_3Z_3-\frac{L_1\lambda_1}{L_3\lambda_2}Z_2+b_4Z_4\right]\mathrm{Exp}[-\mathrm{j}\tilde{K}\cos(\gamma_2)/2]. \tag{46}$$

For the case of S–C–S–F:

$$P_2(\psi,\phi)=\left[Z_1+b_5Z_3+\frac{L_1\lambda_1}{L_3\lambda_2\cosh(\lambda_2)}Z_5-\frac{b_5\cos(\lambda_1)+\sin(\lambda_1)}{\cosh(\lambda_2)}Z_4\right]\mathrm{Exp}[-\mathrm{j}\tilde{K}\cos(\gamma_2)/2]. \tag{47}$$

Therefore, the radiation acoustic pressure of the moderately thick rectangular plate radiator in the flexural vibration in the far field can be obtained as

$$\tilde{P}=-\frac{\tilde{K}\tilde{\rho}_0\tilde{C}_0\beta}{2\pi\tilde{r}}\mathrm{e}^{\mathrm{j}(\beta\tilde{t}-\tilde{K}\tilde{r})}A_1P_1(\psi,\phi)P_2(\psi,\phi). \tag{48}$$

It is seen that the far-field radiation acoustic field of the rectangular Mindlin plate in flexural vibration depends on both the distance and direction. This means that the radiation acoustic field is directional. From Eq. (48), the directivity pattern function can be obtained as

$$D_P=P_1(\psi,\phi)P_2(\psi,\phi). \tag{49}$$

From Eq. (48), it can be seen that the acoustic pressure distribution depends on the geometrical dimensions, the vibrational order of the plate and the frequency. This is somewhat different from the radiation acoustic field of an oscillating piston in an infinite baffle.

4. Comparison study

In order to ascertain the accuracy and reliability of the results presented in this study, a comparison is made with existing results from the literature. Fig. 4 compares the results of the present study with Lin's [13] results, showing the calculated directivity pattern of the simply supported rectangular plate in the flexural vibration.

For numerical computations, the material parameters of the plate (stainless steel) are given as $\rho = 7800\,\mathrm{kg/m^3}$, $\nu = 0.28$ and $E = 195\,\mathrm{GPa}$. The media (air) has the physical constants of $\rho_0 = 1.29\,\mathrm{kg/m^3}$ and $C_0 = 340\,\mathrm{m/s}$. The length, width and thickness of the plate are respectively taken as $a = 0.24\,\mathrm{m}$, $b = 0.16\,\mathrm{m}$ and $h = 0.003\,\mathrm{m}$.

In Fig. 4(b), X and Y denote the spherical coordinates ψ and φ, respectively, and Z denotes the directivity function $D_p(\psi, \varphi)$. In Fig. 4, the results are plotted for the instance when $Z = 100D_p$. From Fig. 4, it can be observed that the present results are in an excellent agreement with those of Lin [13].

5. Results and discussion

The sound pressure parameter obtained from the exact characteristic equation presented in Section 3 has been expressed in dimensionless form as $\tilde{P} = Pa^2\eta h/D$. Herein, all results are presented for rectangular steel plates when $\rho = 7800\,\mathrm{kg/m^3}$, $\nu = 0.28$ and $E = 195\,\mathrm{GPa}$. The media (air) has the physical constants as $\rho_0 = 1.29\,\mathrm{kg/m^3}$ and $C_0 = 340\,\mathrm{m/s}$.

5.1. Effect of nodal line on the directivity pattern

The results given in Figs. 5 and 6 are for different values of thickness to length ratio δ and aspect ratio η. The dimensionless directivity pattern in these figures is illustrated for moderately thick rectangular plate with different combinations of boundary conditions.

As shown in Fig. 5, the directivity pattern of the plate in free flexural vibration is maximum for mode shape $(m, n) = (1, 1)$ when $\psi = 0$. It is expected from Fig. 5 that the directivity patterns of the S–S–S–S square plate are equal for $\varphi = 0, \pi/2, \pi, 3\pi/2$ and 2π. The directivity patterns of the plate in free flexural vibration for mode shape $(m, n) = (2, 1)$ are also shown in Fig. 5. One can observe that there is a nodal line in the mode shape at the middle line of the vibrating plate ($X_1 = 0$). It is expected that this nodal line affects the directivity pattern of the plate. The directivity pattern of the plate is equal to zero because there are two equal positive and negative sound radiations in both sides of the nodal line, as shown in Fig. 5. Furthermore, all values of the

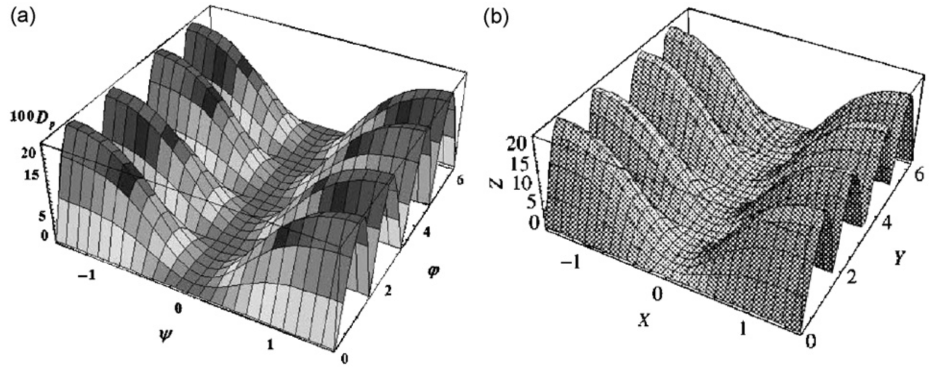

Fig. 4. Comparison study of the directivity pattern parameter for an S–S–S–S rectangular plate ($\delta = 0.0125$ and $\eta = 1.5$): (a) present result (Mindlin plate theory) and (b) Lin [13] (thin plate theory).

Mode Sequence	Directivity Pattern,	$\kappa = \sqrt{0.86667}$
 $(m = 1, n = 1)$	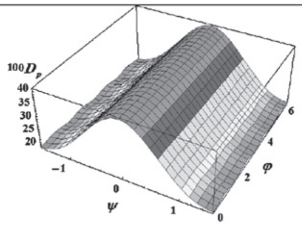 $\delta = 0.1, \eta = 0.5$ $\beta = 12.080555$	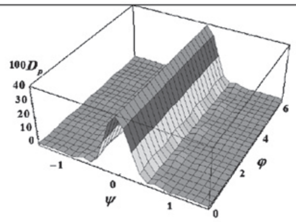 $\delta = 0.1, \eta = 2$ $\beta = 45.655658$
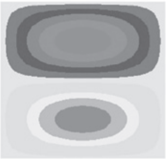 $(m = 2, n = 1)$	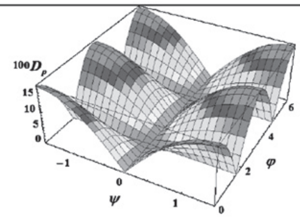 $\delta = 0.01, \eta = 0.5$ $\beta = 41.915032$	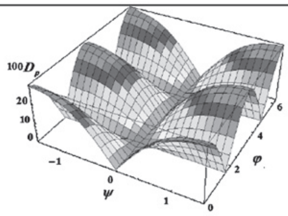 $\delta = 0.01, \eta = 2$ $\beta = 78.847884$
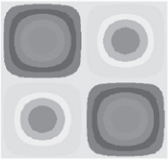 $(m = 2, n = 2)$	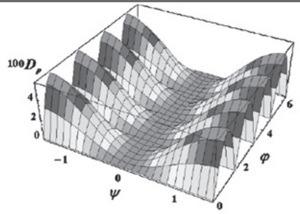 $\delta = 0.01, \eta = 0.5$ $\beta = 49.305422$	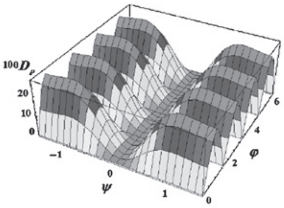 $\delta = 0.01, \eta = 2$ $\beta = 196.713756$

Fig. 5. Calculated three-dimensional acoustic pressure (directivity pattern) of the S–S–S–S rectangular Mindlin plates in free flexural vibration.

directivity pattern of the plate in free flexural vibration are also zero on every circle whose projection is on the nodal line of the plate.

It can be easily deduced from the mode shape $(m, n) = (2, 2)$ that the directivity pattern of the plate in free flexural vibration is equal to zero for $\varphi = 0$, $\pi/2$, π, $3\pi/2$ and 2π. This is due to the fact that there are two different nodal lines at $X_1 = X_2 = 0$. These assumptions are confirmed by the numerical results presented in Fig. 5.

5.2. Effect of boundary conditions on the directivity pattern

In order to study the effects of boundary conditions on the directivity pattern behavior of the plate, we turn attention to Fig. 6. It is observed from Fig. 6 that the directivity pattern in mode shape $(m, n) = (1, 2)$ for moderately thick rectangular plates with S–C–S–S, S–S–S–F and S–C–S–F boundary conditions is not equal to zero for $\psi = 0$. This is due to the fact that the nodal line is moved from $X_2 = 0$ to $X_2 = \varepsilon(\varepsilon \ll 1)$. The directivity pattern of the plates with S–S–S–S, S–C–S–C and S–F–S–F boundary conditions is equal to zero, since the nodal line is set at $X_2 = 0$. Considering the influence of the free boundary conditions on the directivity pattern and comparing three plates with the same values of both the thickness to length ratio δ and aspect ratio η, as well as with the same boundary conditions at three edges (i.e., S–S–S–S, S–C–S–S and S–S–S–F, as presented in Fig. 6), the plate having a free boundary condition on the fourth edge has greater directivity pattern than the plates with clamped or simply supported boundary conditions.

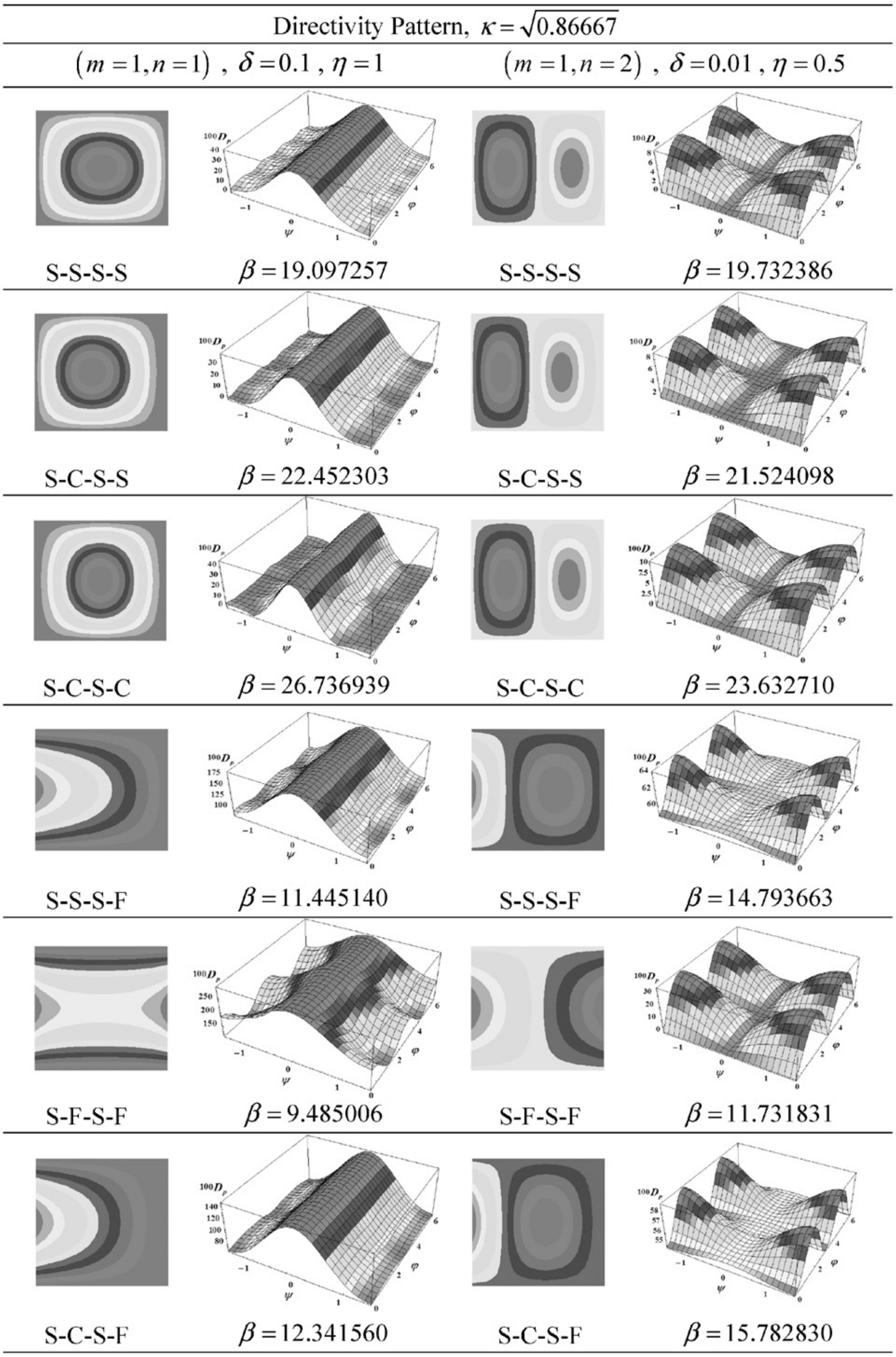

Fig. 6. Three-dimensional directivity pattern for rectangular Mindlin plates in free flexural vibration with six combinations of boundary conditions.

It can also be observed in Fig. 6 that the shape of the directivity pattern does not change for the plates having an identical thickness to length ratio δ, aspect ratio η and mode shape (m, n) when different combinations of boundary conditions are taken into account.

5.3. Effect of thickness to length ratio on the plate parameters

The influence of the thickness to length ratio δ on the plate parameters, including the sound pressure, frequency and critical distance parameters for square plates ($\eta = 1$), with six possible combinations of boundary conditions, is examined in Figs. 7–9. In these figures, $(m, n) = (1, 1)$ while the thickness to length ratio δ varies from 0.001 to 0.2.

It should be noted that Fig. 7 is plotted for $\tilde{r} = 3.5$ at $\Psi = 0$ and $\varphi = \pi/4$. From the results presented in Fig. 7, it can be observed that as the thickness to length ratio δ increases, the sound pressure parameter $\tilde{P}$ decreases. This is because at a higher thickness to length ratio δ, the effect of shear deformation and rotary inertia is more considerable. These effects are also more pronounced in the higher modes than those in the lower modes. Another conclusion that can be deduced from Fig. 7 is the sound pressure parameter $\tilde{P}$ increases when higher degrees of edge constraints are applied to the edges of the plate.

The behavior of the frequency parameter β in Fig. 8 is similar to that of the sound pressure parameter $\tilde{P}$, as shown in Fig. 7. From Fig. 9, it can be concluded that the effect of the higher degrees of edge constraints on the growth rate of the critical distance parameter $\tilde{D}_c$ is more tangible as the thickness to length ratio δ increases from 0.001 to 0.2.

5.4. Effect of aspect ratio on the plate parameters

The effect of the aspect ratio η on the plate parameters, including the sound pressure, frequency and critical distance parameters for rectangular Mindlin plates ($\delta = 0.1$) with six possible combinations of boundary conditions is graphically investigated in Figs. 10–13. In these figures, $(m, n) = (1, 1)$ when the aspect ratio η has values between 0.4 and 2.5.

The curves in Figs. 10 and 11 are depicted for $\tilde{r} = 8$ at $\Psi = 0$ and $\varphi = \pi/4$. The primary conclusion inferred from Figs. 10 and 11 is to increase the sound pressure parameter $\tilde{P}$ with the enhancement of the aspect ratio η. It can also be observed that applying higher degrees of constraints to the edges of the plate leads to the increase of the sound pressure parameter $\tilde{P}$ for any values of the aspect ratio η. It is worthwhile to mention that the sound pressure parameter $\tilde{P}$ for the S–F–S–F rectangular Mindlin plate approaches a constant value as the aspect ratio η value rises. Furthermore, for some ranges of the aspect ratio η, the sound pressure parameter $\tilde{P}$ increases for the S–F–S–F rectangular Mindlin plate when compared with the S–C–S–F one.

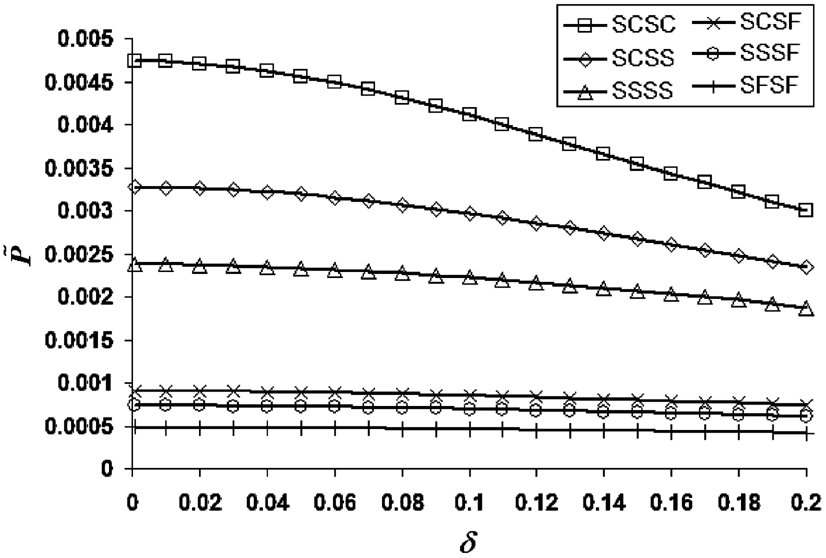

Fig. 7. Variation of sound pressure parameter $\tilde{P}$ versus δ for square Mindlin plates with six combinations of boundary conditions when $(m, n) = (1, 1)$ at $\psi = 0$, $\varphi = \pi/4$ and $\tilde{r} = 3.5$.

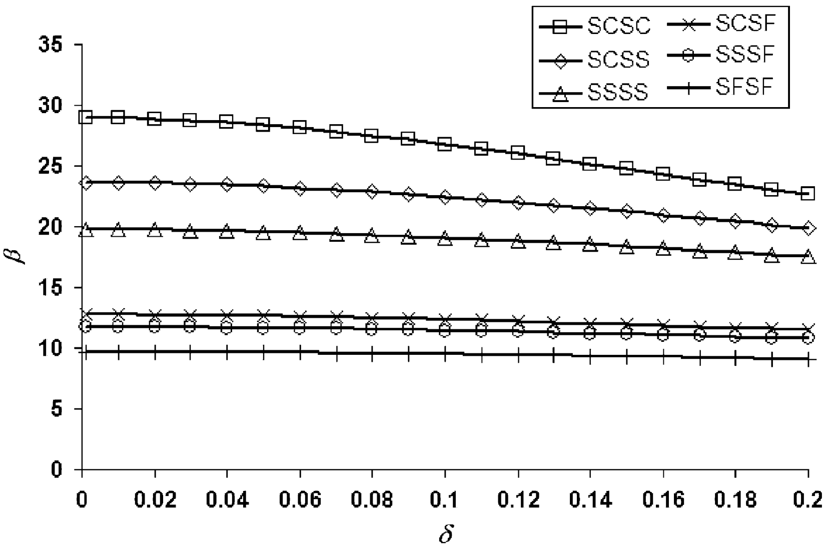

Fig. 8. Variation of frequency parameter β versus δ for square Mindlin plates with six combinations of boundary conditions when $(m, n) = (1, 1)$.

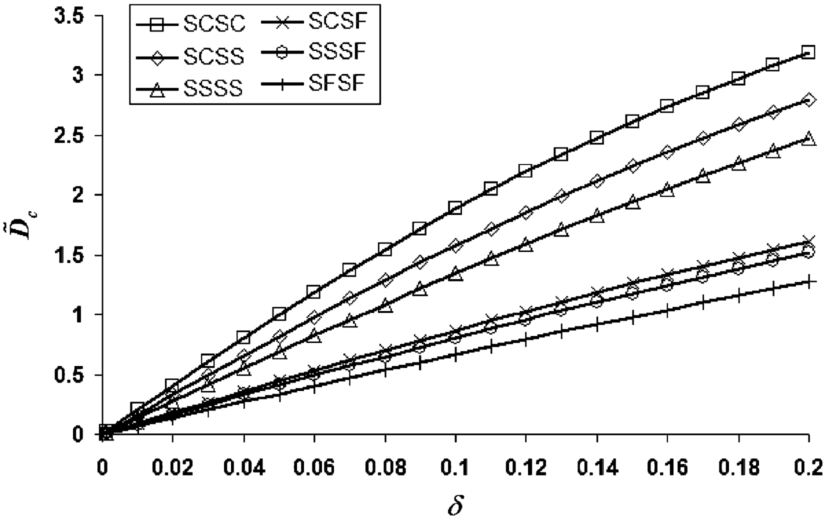

Fig. 9. Variation of critical distance parameter $\tilde{D}_c$ versus δ for square Mindlin plates with six combinations of boundary conditions when $(m, n) = (1, 1)$.

The trend of variation of the plate parameters versus η in both Figs. 12 and 13 is similar to that in Fig. 11 as well as to each other. From Figs. 12 and 13, it can be deduced that the influence of the higher degrees of edge constraints on the growth rate of the frequency parameter β and the critical distance parameter $\tilde{D}_c$ is more considerable with the increase of the aspect ratio η from 0.4 to 2.5.

5.5. Effect of boundary conditions on the sound pressure parameter $(\tilde{P}/A_1\tilde{r})$

In order to study the effect of the six combinations of boundary conditions for square Mindlin plates $(\eta = 1)$ on the sound pressure parameter $(\tilde{P}/A_1\tilde{r})$, Fig. 14 plots a wide range of the thickness to length ratio δ while $(m, n) = (1, 1)$, $\Psi = 0$ and $\varphi = \pi/4$. From the results presented in Fig. 14, it is found that regardless of the boundary conditions, the sound pressure parameter $(\tilde{P}/A_1\tilde{r})$ diminishes with an increase of the thickness to

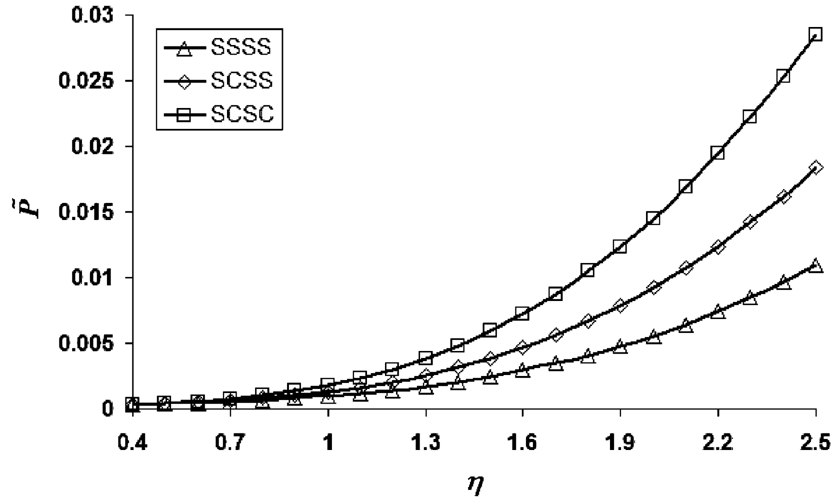

Fig. 10. Variation of sound pressure parameter $\tilde{P}$ versus η for S–S–S–S, S–C–S–S and S–C–S–C rectangular Mindlin plates ($\delta = 0.1$) when $(m,n) = (1,1)$ at $\psi = 0$, $\varphi = \pi/4$ and $\tilde{r} = 8$.

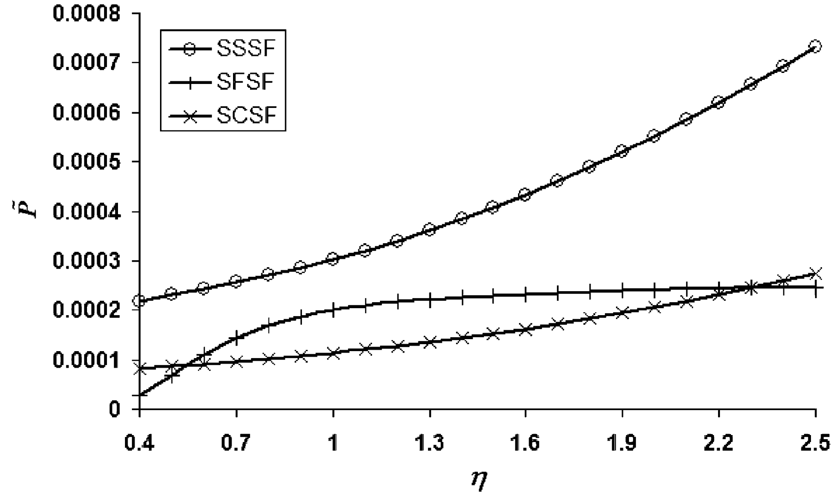

Fig. 11. Variation of sound pressure parameter $\tilde{P}$ versus η for S–S–S–F, S–F–S–F and S–C–S–F rectangular Mindlin plates ($\delta = 0.1$) when $(m,n) = (1,1)$ at $\psi = 0$, $\varphi = \pi/4$ and $\tilde{r} = 8$.

length ratio δ from 0.001 to 0.2. It is worthy noting that for the higher degrees of edge constraints considered for the square plate, the sound pressure parameter $(\tilde{P}/A_1\tilde{r})$ decreases in most ranges of the thickness to length ratio δ. In some boundary conditions, an inverse behaviour is experienced at the switching point ($\delta \leqslant 0.7$) for cases with no free constraints at the edges of the plate. Among all the six boundary conditions considered in Fig. 14, it can be seen that the lowest and highest values of $\tilde{P}/A_1\tilde{r}$ correspond to the S–C–S–C and S–F–S–F cases, respectively. Thus, constraints at the edges increase the flexural rigidity of the plate, resulting in lower sound pressure parameters.

6. Conclusions

In this work, the Mindlin plate theory was used to investigate the acoustic radiation behavior of moderately thick rectangular plates. The exact closed-form sound pressure equations were derived for the six cases having

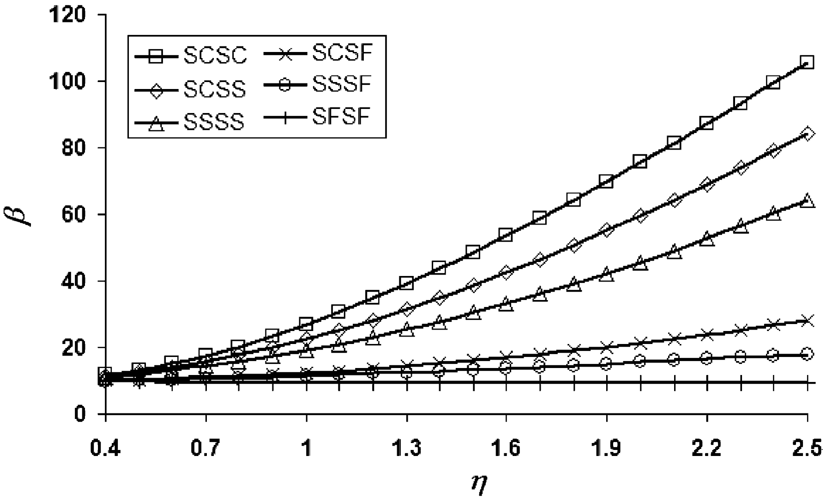

Fig. 12. Variation of frequency parameter β versus η for rectangular Mindlin plates ($\delta = 0.1$) with six combinations of boundary conditions when $(m, n) = (1, 1)$.

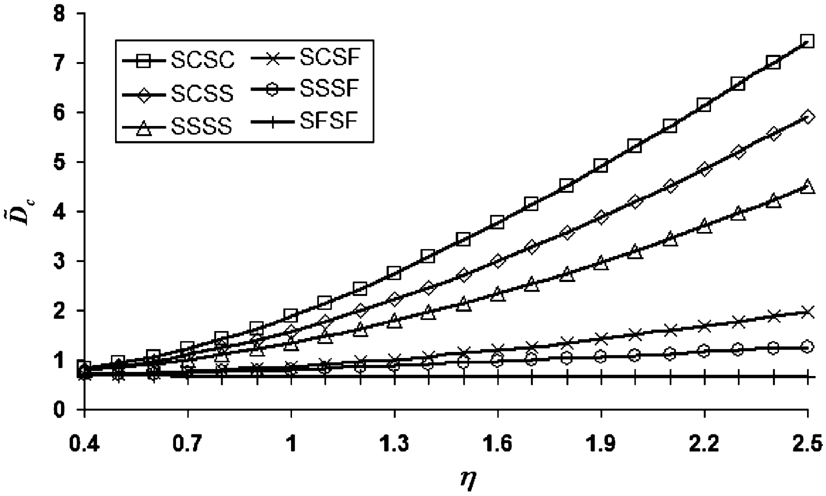

Fig. 13. Variations of critical distance parameter $\tilde{D}_c$ versus η for rectangular Mindlin plates ($\delta = 0.1$) with six combinations of boundary conditions when $(m, n) = (1, 1)$.

two opposite sides simply supported. The six cases considered in the present study include S–S–S–S, S–C–S–S, S–C–S–C, S–S–S–F, S–F–S–F and S–C–S–F rectangular plates. The transverse deflection and displacements along the X_1- and X_2-axes were also given as a closed form for all six cases. To ensure the accuracy of the derived formulations, the results obtained by the present exact analytical solutions have been compared with their counterparts in the literature. The directivity patterns and their associated contour plots at any mode sequence of the plate in free flexural vibration were graphically displayed. Extensive and accurate results of the plate parameters, including the sound pressure, frequency and critical distance parameters for a square plate with six combinations of boundary conditions were presented for a wide range of aspect ratios and thickness to length ratios. Finally, the graph of the sound pressure parameter ($\tilde{P}/A_1\tilde{r}$) versus the thickness to length ratio was illustrated for six combinations of boundary conditions.

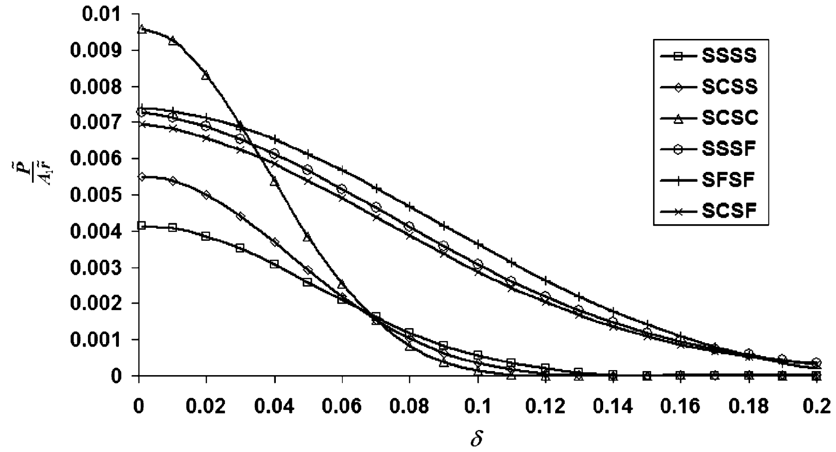

Fig. 14. Variation of sound pressure parameter $\tilde{P}/A_1\tilde{r}$ versus δ for square Mindlin plates with six combinations of boundary conditions when $(m,n)=(1,1)$ at $\psi=0$, $\varphi=\pi/4$.

The main advantages of the exact analytical solutions presented in this paper can be summarized as follows:

- The proposed closed-form acoustic radiation equations are capable of predicting highly accurate sound pressure within the framework of Mindlin plate theory. This is because exact analytical solutions are used to derive and solve the governing differential equations of motion.
- All of the results obtained by the exact analytical solutions provide researchers and designers with a reliable source to validate the numerical results of their own problems.

Appendix A

The governing differential equations based on the Mindlin first-order shear deformation plate theory in the absence of in-plane stress resultants are given by Ref. [17]

$$\nu_1(\tilde{\chi}_{1,11}+\eta^2\tilde{\chi}_{1,22})+\nu_2(\tilde{\chi}_{1,11}+\eta\tilde{\chi}_{2,12})-\frac{12\kappa^2\nu_1}{\delta^2}(\tilde{\chi}_1-\tilde{\chi}_{3,1})=-\frac{\delta^2}{12}\beta^2\tilde{\chi}_1, \tag{A.1}$$

$$\nu_1(\tilde{\chi}_{2,11}+\eta^2\tilde{\chi}_{2,22})+\nu_2(\tilde{\chi}_{1,12}+\eta\tilde{\chi}_{2,22})-\frac{12\kappa^2\nu_1}{\delta^2}(\tilde{\chi}_2-\tilde{\chi}_{3,2})=-\frac{\delta^2}{12}\beta\tilde{\chi}_2, \tag{A.2}$$

$$\frac{12\kappa^2\nu_1}{\delta^2}(\tilde{\chi}_{3,11}+\eta^2\tilde{\chi}_{3,22}-(\tilde{\chi}_{1,1}+\eta\tilde{\chi}_{2,2}))=-\beta^2\tilde{\chi}_3, \tag{A.3}$$

where $\nu_1=(1-\nu)/2$, $\nu_2=(1+\nu)/2$, $\tilde{\chi}_1$ and $\tilde{\chi}_2$ are the rotations of the transverses normal about the X_1- and X_2-axis, respectively, and the symbol "," is used to indicate the partial derivative. For example, $\tilde{\chi}_{3,11}$ is equivalent to $\partial^2\tilde{\chi}_3/\partial x_1^2$ while $\tilde{\chi}_{3,1}$ means $\partial\tilde{\chi}_3/\partial x_1$.

In order to find the displacement, the X_1- and X_2-axes are denoted by $U_1=-X_3\tilde{\chi}_1$ and $U_2=-X_3\tilde{\chi}_2$, respectively, and transverse deflection along the X_3-axis is denoted by $\tilde{U}_3=\tilde{\chi}_3$. Eqs. (A.1)–(A.3) may be solved by introducing the three dimensionless potentials functions W_1, W_2 and W_3 as follow [17]:

$$\tilde{\chi}_1=C_1W_{1,1}+C_2W_{2,1}-\eta W_{3,2}, \tag{A.4}$$

$$\tilde{\chi}_2=C_1\eta W_{1,2}+C_2\eta W_{2,2}+W_{3,1}, \tag{A.5}$$

$$\tilde{\chi}_3=W_1+W_2. \tag{A.6}$$

Based on these dimensionless potentials, the governing equations of motion may now be expressed as

$$W_{1,11}+\eta^2 W_{1,22}=-\alpha_1^2 W_1, \tag{A.7}$$

$$W_{2,11}+\eta^2 W_{2,22}=-\alpha_2^2 W_2, \tag{A.8}$$

$$W_{3,11}+\eta^2 W_{3,22}=-\alpha_3^2 W_3. \tag{A.9}$$

In Ref. [17], the problem is also solved by the method of separation of variables. Thus, the set of suitable solutions satisfying the boundary conditions, when two opposite edges at $X_1=-0.5$ and $X_1=0.5$ are simply supported, may be selected as

$$W_1=[A_1\ \sin(\lambda_1(X_2+0.5))+A_2\ \cos(\lambda_1(X_2+0.5))]\sin(\mu(X_1+0.5)), \tag{A.10}$$

$$W_2=[A_3\ \sinh(\lambda_2(X_2+0.5))+A_4\ \cosh(\lambda_2(X_2+0.5))]\sin(\mu(X_1+0.5)), \tag{A.11}$$

$$W_3=[A_5\ \sinh(\lambda_3(X_2+0.5))+A_6\ \cosh(\lambda_3(X_2+0.5))]\cos(\mu(X_1+0.5)). \tag{A.12}$$

Introducing the three dimensionless potentials functions Eqs. (A.10)–(A.12) in Eqs. (A.4)–(A.6), the three dimensionless functions $\tilde{\chi}_1$, $\tilde{\chi}_2$ and $\tilde{\chi}_3$ are given by

$$\begin{aligned}\tilde{\chi}_1=[&A_1C_1\mu\ \sin(\lambda_1(X_2+0.5))+A_2C_1\mu\ \cos(\lambda_1(X_2+0.5))+A_3C_2\mu\ \sinh(\lambda_2(X_2+0.5))\\&+A_4C_2\mu\ \cosh(\lambda_1(X_2+0.5))-A_5\eta\lambda_3\cosh(\lambda_2(X_2+0.5))\\&-A_6\eta\lambda_3\sinh(\lambda_1(X_2+0.5))]\cos(\mu(X_1+0.5)),\end{aligned} \tag{A.13}$$

$$\begin{aligned}\tilde{\chi}_2=[&A_1C_1\eta\lambda_1\ \cos(\lambda_1(X_2+0.5))-A_2C_1\eta\lambda_1\ \sin(\lambda_1(X_2+0.5))\\&+A_3C_2\eta\lambda_2\ \cosh(\lambda_2(X_2+0.5))+A_4C_2\eta\lambda_2\ \sinh(\lambda_1(X_2+0.5))\\&-A_5\mu\ \sinh(\lambda_3(X_2+0.5))+A_6\mu\ \cosh(\lambda_3(X_2+0.5))]\sin(\mu(X_1+0.5)),\end{aligned} \tag{A.14}$$

$$\begin{aligned}\tilde{\chi}_3=[&A_1\ \sin(\lambda_1(X_2+0.5))+A_2\ \cos(\lambda_1(X_2+0.5))+A_3\ \sinh(\lambda_2(X_2+0.5))\\&+A_4\ \cosh(\lambda_2(X_2+0.5))]\sin(\mu(X_1+0.5)).\end{aligned} \tag{A.15}$$

The remaining six unknown's arbitrary constants A_i are evaluated by means of the two boundary conditions at $X_2=-0.5$ and $X_2=0.5$ and can be simply supported, clamped or free, as show in Fig. 1. Focusing on the arbitrary constants A_i $(i=1,2,\ldots,6)$ and presenting them in terms of A_1, leads to the expressions of the dimensionless displacements for the six combinations of boundary conditions.

Case 1. S–S–S–S:

$$A_2=A_3=A_4=A_5=A_6=0, \tag{A.16}$$

$$\lambda_1=n\pi. \tag{A.17}$$

Case 2. S–C–S–S:

$$A_2=A_4=A_5=0, \tag{A.18}$$

$$A_3=-(\sin(\lambda_1)/\sinh(\lambda_2))A_1, \tag{A.19}$$

$$A_6=((C_1-C_2)\mu\ \sin(\lambda_1)/(\eta\lambda_3\ \sinh(\lambda_3)))A_1. \tag{A.20}$$

Case 3. S–C–S–C:

$$A_2=b_1A_1, \tag{A.21}$$

$$A_3=-((b_1\ \cos(\lambda_1)-b_1\ \cosh(\lambda_2)+\sin(\lambda_1))/\sinh(\lambda_2))A_1, \tag{A.22}$$

$$A_4=-b_1A_1, \tag{A.23}$$

$$A_5=(\mu b_1(C_1-C_2)/(\eta\lambda_3))A_1, \tag{A.24}$$

$$A_6 = ((C_1\eta\lambda_1 \sinh(\lambda_2) - C_2\eta\lambda_2(b_1 \cos(\lambda_1) - b_1 \cosh(\lambda_2) + \sin(\lambda_1)))/(\mu \sinh(\lambda_2)))A_1. \tag{A.25}$$

Case 4. S–S–S–F:

$$A_2 = b_2 A_1, \tag{A.26}$$

$$A_3 = -(L_1\lambda_1/(L_3\lambda_2))A_1, \tag{A.27}$$

$$A_4 = ((L_1\lambda_1 \sinh(\lambda_2)/(L_3\lambda_2) - b_2 \cos(\lambda_1) - \sin(\lambda_1))/\cosh(\lambda_2))A_1, \tag{A.28}$$

$$\begin{aligned} A_5 = {} & (C_2(\mu^2 v - \eta^2\lambda_2^2)(L_1\lambda_1 \sinh(\lambda_2)/(L_3\lambda_2) - b_2 \cos(\lambda_1) - \sin(\lambda_1))/\cosh(\lambda_2) \\ & + b_2 C_1(\mu^2 v + \eta^2\lambda_1^2)/(\mu\eta\lambda_3(v-1))A_1, \end{aligned} \tag{A.29}$$

$$A_6 = 2\mu\eta\lambda_1(C_1 - C_2 L_1/L_3)/(\mu^2 + \eta^2\lambda_3^2)A_1. \tag{A.30}$$

Case 5. S–F–S–F:

$$A_2 = b_3 A_1, \tag{A.31}$$

$$A_3 = -(L_1\lambda_1/(L_3\lambda_2))A_1, \tag{A.32}$$

$$A_4 = b_4 A_1, \tag{A.33}$$

$$A_5 = (C_1 b_3(\mu^2 v + \eta^2\lambda_1^2) + b_4 C_2(\mu^2 v - \eta^2\lambda_2^2))/(\mu\eta\lambda_3(v-1))A_1, \tag{A.34}$$

$$A_6 = \frac{\eta\lambda_1}{\mu}(C_1 - 1 - (C_2 - 1)L_1/L_3)A_1. \tag{A.35}$$

Case 6. S–C–S–F:

$$A_2 = b_5 A_1, \tag{A.36}$$

$$A_3 = -(L_1\lambda_1/(L_3\lambda_2))A_1, \tag{A.37}$$

$$A_4 = ((L_1\lambda_1 \sinh(\lambda_2)/(L_3\lambda_2) - b_5 \cos(\lambda_1) - \sin(\lambda_1))/\cosh(\lambda_2))A_1, \tag{A.38}$$

$$\begin{aligned} A_5 = {} & \big(C_2(\mu^2 v - \eta^2\lambda_2^2)(L_1\lambda_1 \sinh(\lambda_2)/(L_3\lambda_2) - b_5 \cos(\lambda_1) - \sin(\lambda_1))/\cosh(\lambda_2) \\ & + b_5 C_1(\mu^2 v + \eta^2\lambda_1^2)\big)/(\mu\eta\lambda_3(v-1))A_1, \end{aligned} \tag{A.39}$$

$$A_6 = \frac{\eta\lambda_1}{\mu}(C_1 - 1 - (C_2 - 1)L_1/L_3)A_1. \tag{A.40}$$

Using the Eqs. (A.1)–(A.3), it is easy to show the orthogonality relation as

$$A_1 = 1 \Bigg/ \sqrt{\int_{-0.5}^{0.5}\int_{-0.5}^{0.5}\left[\frac{\delta^2}{12}(\bar{\psi}_1^2 + \bar{\psi}_2^2) + \bar{\psi}_3^2\right] \mathrm{d}X_1\,\mathrm{d}X_2}, \tag{A.41}$$

where

$$\tilde{\chi}_1 = A_1\bar{\psi}_1, \tag{A.42}$$

$$\tilde{\chi}_2 = A_1\bar{\psi}_2, \tag{A.43}$$

$$\tilde{\chi}_3 = A_1\bar{\psi}_3. \tag{A.44}$$

References

[1] A.W. Leissa, Vibration of Plates, NASA SP-169, Office of Technology Utilization, NASA, Washington, DC, 1969. Reprinted by The Acoustical Society of America, 1993.

[2] A.W. Leissa, Recent research in plate vibrations: classical theory, *Shock and Vibration Digest* 9 (1977) 13–24.

[3] A.W. Leissa, Recent research in plate vibrations: complicating effects, *Shock and Vibration Digest* 9 (1977) 21–35.
[4] A.W. Leissa, Plate vibration research, 1976–1980: classical theory, *Shock and Vibration Digest* 13 (1981) 11–22.
[5] A.W. Leissa, Plate vibration research, 1976–1980: complicating effects, *Shock and Vibration Digest* 13 (1981) 19–36.
[6] L. Rayleigh, *The Theory of Sound*, second ed., reprinted by Dover, New York, 1945.
[7] N.S. Lomas, S.I. Hayek, Vibration and acoustic radiation of elastically supported rectangular plates, *Journal of Sound and Vibration* 2 (1977) 1–25.
[8] L. Cremer, M. Heckl, *Structure-Borne Sound*, second ed., Springer, New York, 1987, p. 573.
[9] E.G. Williams, A series expansion of the acoustic power radiated from planar sources, *Journal of the Acoustical Society of America* 73 (1983) 1520–1524.
[10] M.R. Lee, R. Singh, Analytical formulations for annular disk sound radiation using structural modes, *Journal of the Acoustical Society of America* 95 (6) (1994) 3311–3323.
[11] J.S. Tao, G.R. Liu, K.Y. Lam, Sound radiation of a thin infinite plate in light and heavy fluids subject to multi-point excitation, *Applied Acoustics* 62 (2001) 573–587.
[12] S. Lin, Acoustic field of flexural circular plates for air-coupled ultrasonic transducers, *Acustica* 86 (2000) 388–391.
[13] S. Lin, Study on the radiation acoustic field of rectangular radiators in flexural vibration, *Journal of Sound and Vibration* 254 (3) (2002) 469–479.
[14] L. Zhou, H. Zheng, K.C. Hung, Sound radiation from a thin infinite plate in contact with a layered inhomogeneous fluid, *Applied Acoustics* 63 (2002) 1177–1192.
[15] T. Musha, Calculation of instantaneous radiation characteristics using the wavelet transform, *Applied Acoustics* 65 (2004) 705–718.
[16] H. Lee, R. Singh, Comparison of two analytical methods used to calculate sound radiation from radial vibration modes of a thick annular disk, *Journal of Sound and Vibration* 285 (4–5) (2005) 1210–1216.
[17] S. Hosseini-Hashemi, M. Arsanjani, Exact characteristic equations for some of classical boundary conditions of vibrating moderately thick rectangular plates, *International Journal of Solids and Structures* 42 (2005) 819–853.
[18] S.M. Kirkup, Computational solution of the acoustic field surrounding a baffled panel by the Rayleigh integral method, *Applied Mathematical Modeling* 18 (7) (1994) 403–407.